Generation of Infrasound by Evaporating Hydrometeors in a Cloud Model

DAVID A. SCHECTER

NorthWest Research Associates, Redmond, Washington

MELVILLE E. NICHOLLS

Cooperative Institute for Research in Environmental Sciences, University of Colorado, Boulder, Colorado

(Manuscript received 19 March 2009, in final form 31 August 2009)

ABSTRACT

The dynamical core of the Regional Atmospheric Modeling System has been tailored to simulate the infrasound of vortex motions and diabatic cloud processes in a convective storm. Earlier studies have shown that the customized model (c-RAMS) adequately simulates the infrasonic emissions of generic vortex oscillations. This paper provides evidence that c-RAMS accurately simulates the infrasound associated with parameterized phase transitions of cloud moisture. Specifically, analytical expressions are derived for the infrasonic emissions of evaporating water droplets in dry and humid environments. The dry analysis considers two single-moment parameterizations of the microphysics, which have distinguishable acoustic signatures. In general, the analytical results agree with the numerical output of the model. An appendix briefly demonstrates the ability of c-RAMS to accurately simulate the infrasound of the entropy and mass sources generated by an equilibrating cloud of icy hydrometeors.

1. Introduction

Recent observations and longstanding theoretical considerations suggest that a developing tornado has a detectable signature in the infrasound[1] of a severe storm (Bedard 2005; Bedard et al. 2004; Georges 1976; Passner and Noble 2006; Szoke et al. 2004). To reliably distinguish the vortex signal from extraneous noise, we must improve our current understanding of the various mechanisms that produce infrasound in atmospheric convection. Without detailed observations of the acoustic sources within a storm, numerical modeling may be the best method of investigation.

On the other hand, standard cloud models were not designed for the study of atmospheric infrasound. Their capabilities and limitations in this area of research are not fully understood. Here, we consider a special version of the Regional Atmospheric Modeling System (RAMS) that has been customized to simulate acoustics (Nicholls and Pielke 2000). Cotton et al. 2003 provide an overview of standard RAMS, whereas details of the microphysics parameterizations can be found in a number of additional papers (Walko et al. 1995, 2000; Meyers et al. 1997; Saleeby and Cotton 2004). Appendix A briefly describes the customized version of the model, which is called c-RAMS hereinafter.

The literature contains some evidence that c-RAMS has an adequate foundation for modeling the infrasound of convective storms. Schecter et al. (2008) recently showed that c-RAMS can simulate the adiabatic generation of infrasound by the Rossby-like waves of substorm-scale vortices. Nicholls and Pielke (1994a,b, 2000) previously showed that c-RAMS can simulate the creation of low-frequency compression waves (30-min Lamb waves) by storm-scale heating. However, no prior study has verified that c-RAMS accurately simulates the infrasound that is generated by phase transitions of moisture in the 0.1–10-Hz frequency band. This critical frequency band is where severe storms are observed to produce abnormally strong and distinct signals (Bedard 2005). In theory, adiabatic vortex motions could account for the observations (Bedard 2005; Schecter et al. 2008). However,

[1] The term ‘‘infrasound’’ refers to sound waves at frequencies less than the lower limit of unimpaired human hearing, which is roughly 20 Hz.

Corresponding author address: David A. Schecter, NorthWest Research Associates, 4118 148th Ave. NE, Redmond, WA 98052. E-mail: schecter@nwra.com

DOI: 10.1175/2009JAMC2226.1

entropy and mass fluctuations associated with phase transitions may also contribute. A recent analytical study concluded that such fluctuations in the moist turbulence of a severe storm are likely to dominate other sources of 0.1-Hz infrasound (Akhalkatsi and Gogoberidze 2009).

In this paper, we illustrate the fundamental mechanism by which phase transitions produce infrasound in c-RAMS. We focus on a conceptually simple paradigm—the evaporation of an isolated, homogeneous cloud of water droplets. Analytical expressions are derived for the acoustic emissions in dry and humid environments. Under sufficiently dry conditions, the evaporation may occur in a few seconds or less. Successful comparison of the analytical results to numerical experiments verifies that the practical output of c-RAMS agrees with the theoretical thermo–acoustics of the model. Such verification helps justify using c-RAMS for future numerical studies of infrasound generated by convective storms.

The remainder of this paper is organized as follows: section 2 presents a relatively simple theory for the acoustic emissions of an evaporating cloud in a dry environment, using two different single-moment microphysics parameterizations. Section 3 compares the analytical results of section 2 with numerical simulations. Section 4 presents a theory for the acoustic emissions of an evaporating cloud in a humid environment, and compares the results with numerical simulations. Section 5 contains a summary and concluding remarks. The appendixes discuss our customization of RAMS, the infrasound of icy hydrometeors, and theoretical subtleties regarding evaporation under humid conditions.

2. Theory of infrasound generated by evaporation in a dry environment

This section derives analytical formulas for the infrasound of an evaporating cloud of water droplets in a dry environment. Different results are obtained for different constraints on the evolution of the droplet size distribution, which are commonly imposed by c-RAMS and other cloud models. The analytical results provide benchmarks for evaluating the ability of c-RAMS to simulate infrasound consistent with its theoretical foundation.

a. The pressure equation

Consider an atmosphere at rest that contains a spherical cloud of water droplets. The cloud is characterized by the liquid mixing ratio

$$r_l(\mathbf{x}, t = 0) = r_{l0}\Theta(\epsilon - |\mathbf{x}|), \tag{1}$$

in which $\mathbf{x}$ is the position vector relative to the center of the cloud, t is time, ϵ is the cloud radius, and Θ is the Heaviside step function. The value of Θ is zero or unity if its argument is negative or positive, respectively.

If the air is subsaturated, the water droplets evaporate. Evaporation cools the air and increases the vapor mixing ratio $r_v(\mathbf{x}, t)$ within the cloud. The combination of local cooling and gaseous mass production generates an outward propagating acoustic pulse. The following derives a formal expression for the pressure perturbation $p'(\mathbf{x}, t)$ associated with the pulse. The derivation is based on the thermo-mechanical core of c-RAMS. For simplicity, the ambient pressure p_0, mass density ρ_0, absolute temperature T_0, and sound speed $c_0 \equiv (c_p p_0/c_v \rho_0)^{1/2}$ are treated as constants. The symbols c_p, c_v, and R represent the specific heat at constant pressure, the specific heat at constant volume, and the gas constant of dry air. In general, a prime or zero subscript denotes a perturbation or basic-state variable, respectively.

We assume that all perturbations are sufficiently weak to justify linearizing the compressible gas dynamics. The linearized mass continuity equation, including a source term due to evaporation, is given by

$$\partial_t \rho' + \rho_0 \nabla \cdot \mathbf{u} = \rho_0 \partial_t r_v, \tag{2}$$

in which ρ is the mass density of the gaseous component of moist air and $\mathbf{u}$ is the velocity field. The linearized momentum equation is

$$\partial_t \mathbf{u} = -\frac{1}{\rho_0} \nabla p', \tag{3}$$

assuming that gravitational effects and viscosity are unimportant over the time scale of interest.

The definition of virtual potential temperature,

$$\theta_v \equiv \frac{p}{R\rho}\left(\frac{p_0}{p}\right)^{R/c_p}, \tag{4}$$

here serves as the equation of state. Linearizing Eq. (4) yields

$$\rho' = \frac{p'}{c_0^2} - \rho_0 \frac{\theta_v'}{\theta_{v0}}. \tag{5}$$

Neglecting diffusion by subgrid eddies and sedimentation, the heat equation in RAMS is approximated by the material conservation of ice–liquid potential temperature, defined by (Tripoli and Cotton 1981)

$$\theta_{\mathrm{il}} \equiv \frac{\theta_v}{1 + 0.61 r_v}\left(1 + \frac{L_{\mathrm{lv}} r_l + L_{\mathrm{iv}} r_i}{c_p \max\{T, 253\,\mathrm{K}\}}\right)^{-1}. \tag{6}$$

Here, L_{lv} is the latent heat of vaporization (per unit mass), L_{iv} is the latent heat of sublimation, r_i is the mixing ratio of ice, and T is the absolute temperature of the air. Taking into consideration that $T > 253$ K, $r_i = 0$, $r_v \ll 1$, $L_{lv} r_l / c_p T \ll 1$, and $r_l' = -r_v'$, the linearized heat equation reduces to

$$\partial_t \theta_v' = \left(0.61 - \frac{L_{lv}}{c_p T_0}\right)\theta_{v0}\partial_t r_v. \tag{7}$$

Taking the time derivative of Eq. (2), and eliminating $\mathbf{u}$, ρ', and θ_v' with Eqs. (3), (5), and (7) yields

$$\partial_{tt} p' - c_0^2 \nabla^2 p' = \rho_0 c_0^2 \left(1.61 - \frac{L_{lv}}{c_p T_0}\right)\partial_{tt} r_v. \tag{8}$$

Note that the factor in parentheses is typically negative and much greater than unity, meaning that evaporative cooling dominates the mass source of the acoustic emission. A formal solution to Eq. (8) in an infinite domain is given by

$$p'(\mathbf{x}, t) = \frac{\rho_0}{4\pi}\left(1.61 - \frac{L_{lv}}{c_p T_0}\right)\int \frac{d^3\mathbf{y}}{|\mathbf{x} - \mathbf{y}|}\partial_{tt} r_v(\mathbf{y}, \hat{t}), \tag{9}$$

in which $\hat{t} \equiv t - |\mathbf{x} - \mathbf{y}|/c_0$ is the retarded time. The reader may consult appendix B for a generalization of Eq. (8) that accounts for ice.

b. *Evaporation equations for two single-moment schemes*

Neglecting the convective component of the material derivative, which is second order in the velocity and mixing ratio, the rate of change of water vapor is given by

$$\partial_t r_v = \mu(r_{*c} - r_v)\Theta(\epsilon - |\mathbf{x}|)\Theta(t), \tag{10}$$

in which r_{*c} is the saturation mixing ratio at the surface of a cloud droplet. The bulk rate of evaporation is largely determined by the value of

$$\mu(t) = 4\pi\psi S N D_m, \tag{11}$$

in which ψ is the vapor diffusivity, N is the number concentration of cloud droplets, D_m is the mean droplet diameter, and S is the droplet shape parameter. Here, we have neglected a small correction to μ associated with the characteristic Reynolds number of the droplet motion. To close the evaporation equation [Eq. (10)], μ and r_{*c} must be expressed as functions of r_v.

The first step of the μ closure is to consider the relationship between r_l, N, and D_m. In RAMS, the probability distribution of the droplet diameter D is given by

$$f = \frac{1}{\Gamma(\nu)}\left(\frac{\nu D}{D_m}\right)^{\nu - 1}\frac{\nu}{D_m}e^{-\nu D/D_m}, \tag{12}$$

in which ν is an adjustable parameter and Γ is the standard gamma function. The mass density of cloud droplets is given by $\rho_c = N\int_0^\infty (dD \times fm)$, in which m is the mass of an individual droplet. By assumption, $m = \alpha D^\beta$, in which α and β are empirical parameters. The mixing ratio of cloud water is thus

$$r_l = \frac{\rho_c}{\rho_0} = \frac{N}{\rho_0}\alpha\left(\frac{D_m}{\nu}\right)^\beta \frac{\Gamma(\nu + \beta)}{\Gamma(\nu)}. \tag{13}$$

In a single-moment model, either N or D_m is specified as a fixed parameter of the hydrometeor distribution. An expression for the other parameter as a function of r_v in the evaporating cloud is obtained from Eq. (13) and the conservation of water mass ($r_l' = -r_v'$). Substituting the result into Eq. (11) yields

$$\mu = 4\pi\psi S \begin{cases} N^{(\beta-1)/\beta}\left[\dfrac{\rho_0 \nu^\beta \Gamma(\nu)}{\alpha\Gamma(\nu + \beta)}\right]^{1/\beta}(r_t - r_v)^{1/\beta}, & \dot{N} = 0, \\ \left(\dfrac{\nu}{D_m}\right)^{\beta - 1}\dfrac{\rho_0 \Gamma(\nu)\nu}{\alpha\Gamma(\nu + \beta)}(r_t - r_v), & \dot{D}_m = 0, \end{cases} \tag{14}$$

in which $r_t \equiv r_{v0} + r_{l0}$ and r_{v0} is the initial vapor mixing ratio. Although the constant-N model (top) may seem more physical for the problem under consideration, the constant-D_m model (bottom) is often used for precipitating hydrometeors.

To determine r_{*c}, we suppose that the net heat flux (conductive plus latent) at the surface of each cloud droplet is approximately zero. This leads to an equation of the form

$$L_{lv}\psi\rho(r_{*c} - r_v) = \kappa(T - T_c), \tag{15}$$

in which T_c is the temperature at the surface of a droplet and κ is the thermal conductivity of air (e.g. Pruppacher and Klett 1997). In this section, we simplify Eq. (15) by assuming

$$r_t \ll r_{*c}, \tag{16}$$

which makes sense only for low-density clouds in dry environments. The condition in Eq. (16) permits setting r_v equal to zero on the left-hand side of Eq. (15). We further assume that the liquid water mass is sufficiently small for all other variables in the equation to stay nearly fixed over the course of evaporation. A standard analytical formula for $T_c(r_{*c}, p_0)$ (e.g., Emanuel 1994; Walko et al. 1995) may then be used to convert Eq. (15) into a time-invariant equation for r_{*c}.

Substituting Eq. (14) and a constant value of r_{*c} into Eq. (10) yields an autonomous, first-order, ordinary differential equation (ODE) for r_v. Assuming again that the air remains sufficiently dry throughout the evaporation process [Eq. (16)], we replace $r_{*c} - r_v$ with r_{*c} on the right-hand side. The solution of the ODE for the constant-N model is then

$$r_v = r_{l0}[1 - (1 - \gamma t)^{\beta/(\beta-1)}]\Theta(t)\Theta(1 - \gamma t)\Theta(\epsilon - |\mathbf{x}|) + r_{l0}\Theta(\gamma t - 1)\Theta(\epsilon - |\mathbf{x}|), \quad (17)$$

in which

$$\gamma \equiv 4\pi\psi S \frac{\beta - 1}{\beta}\left(\frac{N}{r_{l0}}\right)^{(\beta-1)/\beta}\left[\frac{\rho_0 \nu^\beta \Gamma(\nu)}{\alpha\Gamma(\nu + \beta)}\right]^{1/\beta} r_{*c}. \quad (18)$$

Here (and below), we have assumed an initial vapor mixing ratio of $r_{v0} = 0$, which corresponds to the numerical experiments of section 3. Note that evaporation ends ($r_v = r_{l0}$) at $t = \gamma^{-1}$. The solution of the ODE for the constant-D_m model is given by

$$r_v = r_{l0}(1 - e^{-\gamma t})\Theta(t)\Theta(\epsilon - |\mathbf{x}|), \quad (19)$$

in which

$$\gamma \equiv 4\pi\psi S\left(\frac{\nu}{D_m}\right)^{\beta-1}\frac{\rho_0\Gamma(\nu)\nu}{\alpha\Gamma(\nu + \beta)} r_{*c}. \quad (20)$$

In this case, evaporation continues forever.

c. *Solutions of the pressure equation*

Given either of the above formulas for r_v, the integral equation for the pressure perturbation [Eq. (9)] is readily evaluated. Consider a spherical coordinate system whose origin is at the observation point, which is a distance x from the center of the cloud. Let ϖ, λ, and φ denote the radius, azimuth, and polar angle (measured from the axis connecting the origin and the center of the cloud). In this coordinate system, we may write $\partial_{tt} r_v \equiv P(t)\Theta(\epsilon - y)$, in which $y \equiv (x^2 + \varpi^2 - 2x\varpi\cos\varphi)^{1/2}$. The specific form of P depends on the single-moment model that is used for the microphysics. Both the constant-N (top) and constant-D_m (bottom) forms are given below:

$$P = \begin{cases} \dfrac{\beta\gamma r_{l0}}{\beta - 1}(1 - \gamma t)^{1/(\beta-1)}\left[\delta(t) - \dfrac{\gamma}{\beta - 1}\dfrac{\Theta(t)\Theta(1 - \gamma t)}{1 - \gamma t}\right], \\ \gamma r_{l0}[\delta(t) - \gamma e^{-\gamma t}\Theta(t)], \end{cases} \quad (21)$$

in which δ is the Dirac distribution. The top and bottom definitions of γ are given by Eqs. (18) and (20), respectively.

Continuing, let $B \equiv \rho_0(1.61 - L_{\mathrm{lv}}/c_p T_0)/4\pi$. Then the integral equation [Eq. (9)] may be written

$$p'(x, t) = B\int_0^\infty d\varpi \int_0^\pi d\varphi \int_0^{2\pi} d\lambda\, \varpi \sin\varphi P(\hat{t})\Theta(\epsilon - y), \quad (22)$$

in which $\hat{t} = t - \varpi/c_0$. Upon further reduction, we obtain

$$p'(x, t) = \frac{\pi B}{x}\int_{x-\epsilon}^{x+\epsilon} d\varpi P(\hat{t})[\epsilon^2 - (x - \varpi)^2], \quad (23)$$

under the assumption that $x > \epsilon$. What remains is to substitute (21) into (23) with $t \to \hat{t}$, and to perform the integration.

The solutions are conveniently expressed in terms of the following dimensionless variables:

$$\tilde{x} \equiv \frac{x}{\epsilon}, \quad \tau \equiv \frac{c_0 t - x}{\epsilon},$$
$$\tilde{\gamma} \equiv \frac{\epsilon}{c_0}\gamma, \quad \text{and} \quad \mathcal{L} \equiv \left(\frac{L_{\mathrm{lv}}}{c_p T_0} - 1.61\right)\frac{r_{l0}}{4}. \quad (24)$$

For the case of evaporation with constant N we have

$$p' = \rho_0 c_0^2 \frac{\mathcal{L}}{\tilde{x}}\frac{\tilde{\gamma}\beta}{\beta - 1}F(\tau, \tilde{\gamma}, \beta), \quad (25)$$

in which

$$F \equiv \begin{cases} F_1 + (\tau^2 - 1)\Theta(1 - |\tau|), & -1 < \tau < \dfrac{\tilde{\gamma} + 1}{\tilde{\gamma}}, \\ 0 & \text{otherwise}, \end{cases} \quad (26)$$

and

$$F_1 \equiv \int_{\max\{-1, \tau - (1/\tilde{\gamma})\}}^{\min\{1, \tau\}} ds \frac{\tilde{\gamma}(1 - s^2)}{\beta - 1}[1 - \tilde{\gamma}(\tau - s)]^{(2-\beta)/(\beta-1)}. \quad (27)$$

The value of F_1 for any τ is obtained by numerical quadrature. For the case of evaporation with constant D_m we have

$$p' = \rho_0 c_0^2 \frac{4\mathcal{L}}{\tilde{x}}\tilde{\gamma}^{-1}G(\tau, \tilde{\gamma}), \quad (28)$$

in which

$$G \equiv \begin{cases} (\tilde{\gamma}\cosh\tilde{\gamma} - \sinh\tilde{\gamma})e^{-\tilde{\gamma}\tau}, & \tau \geq 1, \\ \dfrac{1 + \tilde{\gamma}}{2}e^{-\tilde{\gamma}(\tau+1)} + \dfrac{\tilde{\gamma}\tau}{2} - \dfrac{1}{2}, & -1 < \tau < 1, \\ 0 & \tau \leq -1. \end{cases} \quad (29)$$

Section 3 discusses the basic properties of solutions (25) and (28), and the extent to which they agree with the infrasound that is simulated by c-RAMS.

3. C-RAMS simulations of infrasound generated by evaporation in a dry environment

The analytical pressure perturbations of section 2 are now compared with the infrasound simulated by c-RAMS

TABLE 1. Common experimental parameters, defined in the text.

Parameters	Values
ϵ, c_0	200 m, 347.2 m s^{-1}
p_0, ρ_0	10^5 Pa, 1.16 kg m^{-3}
T_0	300 K
α, β, ν, S	524 kg m^{-3}, 3, 1, 0.5
ψ	2.56×10^{-5} m^2 s^{-1}
κ	0.0262 J m^{-1} s^{-1} K^{-1}
L_{lv}	2.5×10^6 J kg^{-1}
R, c_p, c_v	287, 1004, 717 J kg^{-1} K^{-1}
r_{*0}, $(\partial r_*/\partial T)_0$	2.28×10^{-2}, 1.4×10^{-3} K^{-1}
$dz = dx_i$, dx_o	20, 60 m
dt_i, dt_o	0.02, 0.04 s
X_i, X_o, Z	2.02, 7.92, 8 km

when a cloud evaporates in a dry environment. We consider six numerical experiments with variable microphysics. The common experimental settings (of interest) are listed in Table 1.

A subset of the parameters in Table 1 pertains to the discretization. The model is configured to contain a fine inner grid (i) and a coarse outer grid (o). The inner horizontal grid spacing ($dx_i = dx_o/3$) is one-tenth of the cloud radius ϵ. The vertical grid spacing ($dz = dx_i$) is uniform. Both the inner and outer grids have sufficient spatial resolutions to simulate 1-s (and longer) thermo-acoustic processes; the temporal resolutions ($dt_i = dt_o/2 = 0.02$ s) are also adequate. The horizontal widths of the inner and outer grids (X_i and X_o) are roughly 10 and 40 times ϵ, respectively. The lateral boundary conditions of the outer grid are set to allow free passage of acoustic waves (cf. Klemp and Wilhelmson 1978). The vertical boundaries at the ground and height Z are purely reflective; however, they are far enough removed from the cloud to prevent echoes from returning over the time period under consideration.

The basic state of the atmosphere is dry and isentropic. The vertical density and pressure gradients that would ordinarily appear, because of enforcement of hydrostatic balance, are eliminated by setting the gravitational acceleration g to a very small value (10^{-4} m s^{-2}). At $t = 0$, a cloud is introduced by adding a uniform spherical distribution of r_l [Eq. (1)] in the center of the domain, and adjusting the ice–liquid potential temperature [Eq. (6)] accordingly. In principle, either ''cloud water'' or ''rain'' (two distinct hydrometeor categories in RAMS) may be used to form the cloud mass. Here, we use a customized rain category, which has zero fall speed and an initial temperature of $T_c = 281.2$ K, which corresponds to a surface saturation mixing ratio of $r_{*c} = 6.8 \times 10^{-3}$.

All six experiments use Marshall–Palmer distributions ($\nu = 1$) for the droplet size. The distributions have three distinct initial conditions, summarized in rows 1–3 of Table 2. For each initial condition, the cloud is allowed to

TABLE 2. Distinct initial conditions for experiments in dry (rows 1–3) and humid (rows 4–6) environments. All parameters are defined in sections 2 and 4.

Initial condition	N (m^{-3})	D_m (μm)	r_{v0}/r_{*0}	r_{l0}	ζ_0
1	10^8	11.9	0	4.6×10^{-4}	0.089
2	10^7	25.6	0	4.6×10^{-4}	0.089
3	10^6	55.2	0	4.6×10^{-4}	0.089
4	10^8	11.9	0.9	4.6×10^{-4}	0.89
5	10^7	25.6	0.9	4.6×10^{-4}	0.89
6	5×10^7	25.6	0.95	2.28×10^{-3}	8.9

evaporate keeping either N or D_m fixed. Figure 1 shows the acoustic emission (diamonds) for each case at $x = 424.3$ m. The pressure perturbation is multiplied by $\tilde{x}$ to compensate for ''geometric decay'' with distance from the edge of the cloud.

The top row of Fig. 1 shows the variation of the acoustic emission with the number density N, when N is held fixed during evaporation. Decreasing N by two orders of magnitude severely damps the peak wave amplitude. Although reducing N has little influence on the width of the leading (negative) pulse, it dramatically widens the trailing (positive) wave. The bottom row shows the variation of the acoustic emission with the mean droplet diameter D_m, when D_m is held fixed during evaporation. Each plot is directly underneath the constant-N experiment with the same microscopic initial conditions (Table 2). Evidently, changing the single-moment scheme significantly modifies the shape of the trailing wave, but not the characteristic amplitude or time scale of the emission.

The basic properties of the acoustic emissions are readily explained. To begin with, the leading pulse is created by the initial shock of the evaporation rate over the entire cloud. Because of the finite propagation speed of acoustic signals, an observer senses this shock over a time period of $2\epsilon/c_0$. The duration of the trailing wave is the evaporation time scale, which dilates with decreasing N or increasing D_m. Finally, since the amplitude of the acoustic source decreases with the evaporation rate, so must the emission attenuate with decreasing N or increasing D_m, for a given r_{l0} [see Eq. (14)].

The solid curves in each figure correspond to the integral on the right-hand side of Eq. (22), with $P(\hat{t})$ given by the simulated time series of r_v. All solid curves very closely match the pressure waves that are generated by c-RAMS. In this sense, c-RAMS correctly simulates the infrasound of evaporation.[2]

[2] A similar test has verified the simulated infrasound of evaporation governed by the two-moment microphysics option of c-RAMS (Meyers et al. 1997). In this case, the trailing wave exhibits gradual decay at late times, qualitatively similar to the infrasound generated with fixed D_m.

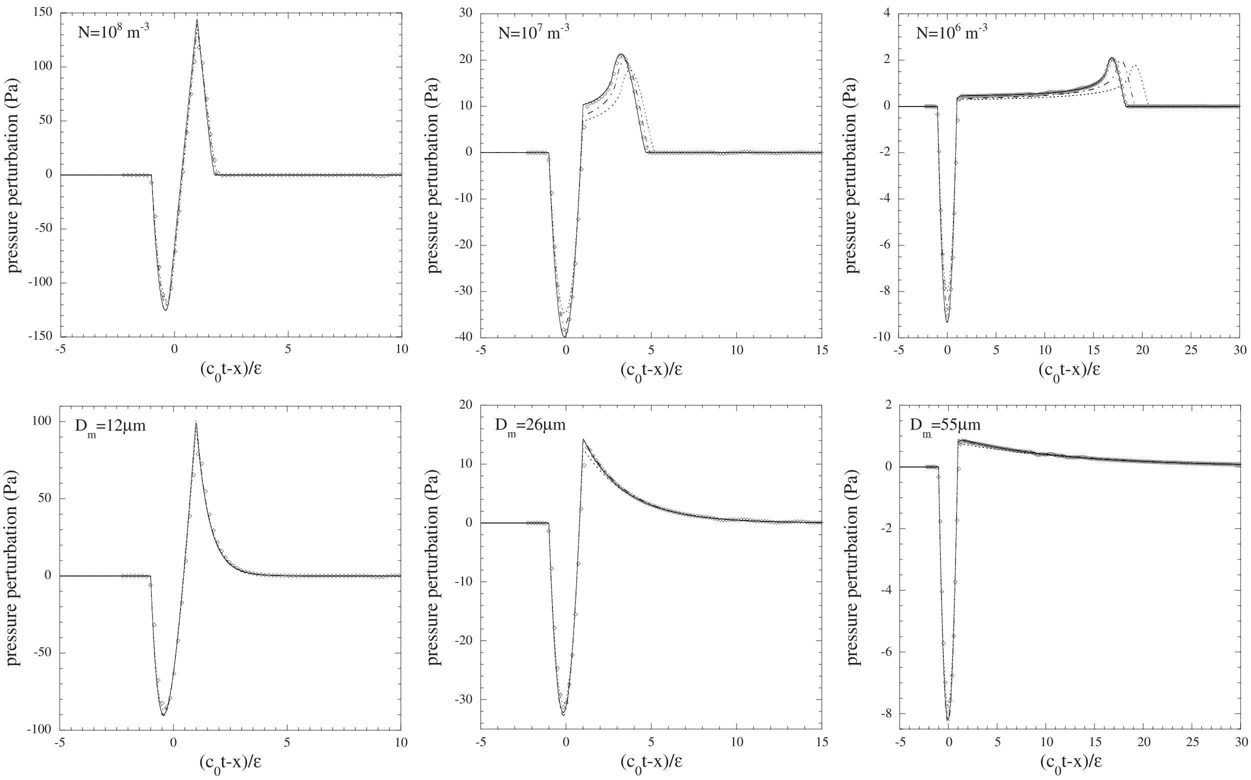

FIG. 1. The infrasound of an evaporating cloud in a dry environment, with six different microphysics parameterizations. (top) Experiments with fixed N (as indicated) and time-dependent D_m. (bottom) Experiments with fixed D_m (as indicated) and time-dependent N. Each column has the same initial values for N and D_m. Diamonds correspond to the infrasound simulated by c-RAMS (only a fraction of the data is shown for clarity). The solid curve corresponds to the infrasound that is theoretically generated by the output time series of r_v. The dotted and dash–dotted curves correspond to two variants of an analytical model that predicts both r_v and p' (see text). The pressure perturbations are multiplied by $\tilde{x} \equiv x/\epsilon$. Note that one unit of $\tau \equiv (c_0 t - x)/\epsilon$ corresponds to a 0.58-s change of t.

The dotted curves in each figure correspond to the analytical approximations of section 2 [Eqs. (25) and (28)]. When D_m is held constant during evaporation, the approximations are excellent. When N is held constant during evaporation, a quantitative discrepancy is noticeable. The error appears primarily because our calculated value of T_c, based on Eq. (15) with $r_v = 0$, is roughly 1 K less than the time-averaged hydrometeor temperature ($\overline{T}_c$) in c-RAMS. The associated 5% discrepancy in $T - T_c$ is plausible, since the vapor mixing ratio grows with time, and the microphysics algorithm in c-RAMS does not strictly enforce Eq. (15) (Walko et al. 2000). The dash–dotted curves are the analytical approximations using $\overline{T}_c$. For fixed N, this revision clearly improves the quantitative agreement between the analytical waves and the infrasound that is generated by c-RAMS. For fixed D_m, the revised curves are nearly indistinguishable from the data.

4. Infrasound generated by evaporation in a humid environment

This section examines the infrasound of an evaporating cloud in a humid environment. For analytical convenience, we restrict our analysis to the single-moment parameterization in which D_m is constant.

a. Basic theory

Factoring μ into two parts, we may rewrite the evaporation equation as follows:

$$\partial_t r_v = \mu_0 (r_t - r_v)(r_{*c} - r_v)\Theta(\epsilon - |\mathbf{x}|)\Theta(t), \tag{30}$$

in which

$$\mu_0 \equiv 4\pi\psi S \left(\frac{\nu}{D_m}\right)^{\beta-1} \frac{\rho_0 \Gamma(\nu)\nu}{\alpha\Gamma(\nu+\beta)}. \tag{31}$$

If the air is nearly saturated, the term $r_{*c} - r_v$ on the right-hand side of Eq. (30) can change over time by a large fraction of its initial value. We may express this term as a function of the variable r_v alone, by substituting the following approximations into Eq. (15):

$$T = T_0 - \frac{L_{\mathrm{lv}}}{c_p}(r_v - r_{v0}) \quad \text{and}$$

$$T_c = T_0 + \left(\frac{\partial r_*}{\partial T}\right)_0^{-1} (r_{*c} - r_{*0}), \tag{32}$$

in which r_{*0} and $(\partial r_*/\partial T)_0$ are the saturation mixing ratio and its temperature derivative at constant pressure, evaluated at T_0 and p_0. The new version of Eq. (15) is given by

$$r_{*c} - r_v = \frac{1+b}{1+a}\left(\frac{r_{*0} + br_{v0}}{1+b} - r_v\right), \tag{33}$$

in which

$$a \equiv \frac{L_{\mathrm{lv}}\psi\rho_0}{\kappa}\left(\frac{\partial r_*}{\partial T}\right)_0 \quad \text{and} \quad b \equiv \frac{L_{\mathrm{lv}}}{c_p}\left(\frac{\partial r_*}{\partial T}\right)_0. \tag{34}$$

The reader may consult appendix C for further discussion of the key approximations used in deriving this result.

The solution of Eq. (30) is conveniently expressed in terms of the following two variables, related to the initial degree of subsaturation and the initial liquid mixing ratio:

$$\xi_0 \equiv r_{*0} - r_{v0} \quad \text{and} \quad \zeta_0 \equiv \frac{(1+b)r_{l0}}{\xi_0}. \tag{35}$$

Specifically, we have

$$r_v = r_{v0}\Theta(|\mathbf{x}| - \epsilon) + [r_{v0}\Theta(-t) + Q(t)\Theta(t)]\Theta(\epsilon - |\mathbf{x}|), \tag{36}$$

in which

$$Q \equiv r_{*0} - \xi_0 \frac{\xi_0 - r_{l0}(1 + be^{-\gamma t})}{\xi_0 - r_{l0}(1+b)e^{-\gamma t}}, \tag{37}$$

and

$$\gamma \equiv \frac{\mu_0}{1+a}\xi_0(1-\zeta_0). \tag{38}$$

The value of γ can be positive or negative. When γ is positive ($\zeta_0 < 1$), the cloud fully evaporates over time. When γ is negative ($\zeta_0 > 1$), saturation occurs before the condensate is fully removed. In this case, the final value of the liquid mixing ratio is $r_{lf} = r_{l0} - \xi_0/(1+b)$. Note that ζ_0 is the ratio of the initial liquid water mass (r_{l0}) to the maximum that can evaporate ($r_{l0} - r_{lf}$).

As before, we may use Eq. (23) to calculate the pressure perturbation outside of the cloud. Solving the integral yields

$$p' = \rho_0 c_0^2 \frac{2\mathcal{L}}{\tilde{x}}\frac{1-\zeta_0}{\zeta_0}\left[\frac{\Theta(\tau+1)}{1-\zeta_0 e^{-\tilde{\gamma}(\tau+1)}} + I(\tau, \tilde{\gamma}, \zeta_0)\right], \tag{39}$$

in which

$$I \equiv \begin{cases} \dfrac{1}{1-\zeta_0 e^{-\tilde{\gamma}(\tau-1)}} + \dfrac{1}{\tilde{\gamma}}\ln\left[\dfrac{e^{\tilde{\gamma}(\tau-1)} - \zeta_0}{e^{\tilde{\gamma}(\tau+1)} - \zeta_0}\right], & \tau \ge 1, \\ \dfrac{\tau}{1-\zeta_0} + \dfrac{1}{\tilde{\gamma}}\ln\left[\dfrac{1-\zeta_0}{e^{\tilde{\gamma}(\tau+1)} - \zeta_0}\right], & -1 < \tau < 1, \\ 0 & \tau \le -1. \end{cases} \tag{40}$$

The dimensionless variables $\tilde{x}$, τ, $\tilde{\gamma}$, and $\mathcal{L}$ were defined earlier in Eq. (24).

The wave form is similar to the acoustic pulse generated by evaporation in a dry environment. A negative minimum occurs at about $\tau = 0$, whereas a positive maximum occurs at $\tau = 1$. If $\tilde{\gamma} \ll 1$, one may derive the following expressions for the minimum (−) and maximum (+) values of the pressure perturbation:

$$p_- = -\frac{3}{16\pi x}\left(\frac{L_{\mathrm{lv}}}{c_p T_0} - 1.61\right)M_{c0}\left(\frac{c_0}{\epsilon}\hat{E}_0\right) \quad \text{and}$$

$$p_+ = \frac{1}{4\pi x}\left(\frac{L_{\mathrm{lv}}}{c_p T_0} - 1.61\right)(1+\zeta_0)M_{c0}\hat{E}_0^2. \tag{41}$$

Here, we have introduced the (approximate) initial cloud mass,

$$M_{c0} \equiv \frac{4\pi\epsilon^3}{3}\rho_0 r_{l0}, \tag{42}$$

and the initial decay rate of the cloud mass,

$$\hat{E}_0 \equiv \frac{1}{r_{l0}}\left(\frac{\partial r_v}{\partial t}\right)_{t=0} = \frac{\mu_0\xi_0}{1+a}. \tag{43}$$

Note that p_+ depends on the cloud size (ϵ) only through M_{c0}, and is proportional to the square of $\hat{E}_0$. Because a cloud-size shock creates the leading wave, p_- varies with ϵ through both M_{c0} and c_0/ϵ, which is the regularized shock frequency. In contrast to p_+, the variation of p_- with $\hat{E}_0$ is linear.

The decay rate (characteristic frequency) of the trailing wave corresponds to the "proper" evaporation rate, defined by

$$E_0 \equiv \frac{1}{r_{l0} - r_{l\infty}}\left(\frac{\partial r_v}{\partial t}\right)_{t=0} = \frac{\mu_0\xi_0}{1+a}\max\{1, \zeta_0\}, \tag{44}$$

in which $r_{l\infty}$ is the time-asymptotic liquid mixing ratio. If the air saturates without consuming the entire cloud, then $r_{l\infty}$ is nonzero and $E_0 > \hat{E}_0$. Figure 2 illustrates how E_0 varies with relative humidity, liquid water mass,

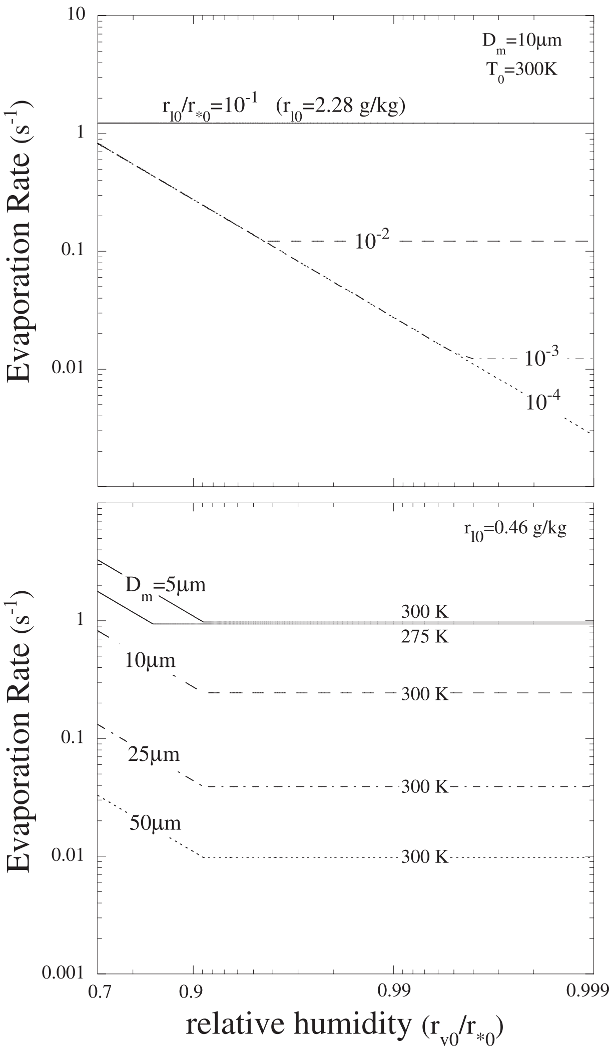

FIG. 2. (top) The characteristic evaporation rate (E_0) vs relative humidity (RH), for several values of the liquid mixing ratio r_{l0}. All curves are calculated with $D_m = 10\ \mu$m, $T_0 = 300$ K, and $p_0 = 10^5$ Pa. (bottom) Evaporation rate E_0 vs RH for several values of the mean droplet diameter D_m. All curves are calculated with $r_{l0} = 4.6 \times 10^{-4}$, $T_0 = 300$ K, and $p_0 = 10^5$ Pa, except for the lower solid (5 μm) curve, in which $T_0 = 275$ K and $p_0 = 73\ 757$ Pa.

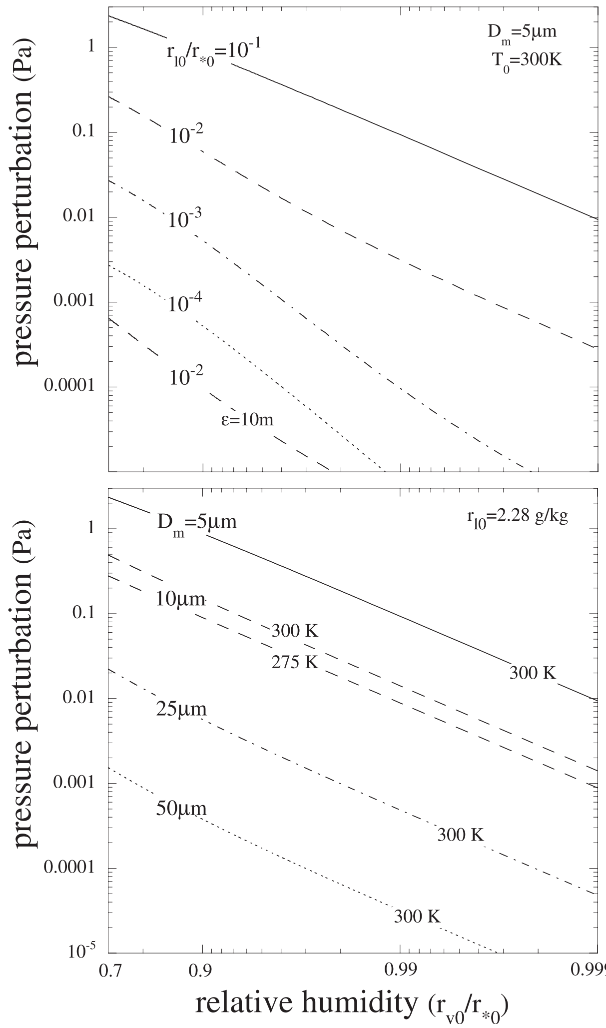

FIG. 3. (top) The pressure peak of the trailing wave at $x = 10$ km vs RH, for several values of the liquid mixing ratio r_{l0}. All curves are calculated with a cloud radius of $\epsilon = 100$ m, except for the lower dashed ($r_{l0} = 0.01 r_{*0}$) curve, for which $\epsilon = 10$ m. Furthermore, all curves are calculated with $D_m = 5\ \mu$m, $T_0 = 300$ K, and $p_0 = 10^5$ Pa. (bottom) The pressure peak of the trailing wave at $x = 10$ km vs RH for several values of the mean droplet diameter D_m. All curves are calculated with $\epsilon = 100$ m, $r_{l0} = 2.28 \times 10^{-3}$, $T_0 = 300$ K, and $p_0 = 10^5$ Pa, except for the lower dashed (10 μm) curve, for which $T_0 = 275$ K and $p_0 = 73\ 757$ Pa.

droplet size, and air temperature.[3] In general, increasing the relatively humidity (r_{v0}/r_{*0}) reduces the evaporation rate until ζ_0 exceeds unity, after which E_0 remains constant. For fixed relative humidity, the evaporation rate decays with the liquid water mass until ζ_0 drops below unity. The evaporation rate also decays with increasing droplet size, as D_m^{-2} if $\beta = 3$. As a final remark on the matter, lowering the air temperature (with an adiabatic pressure drop) tends to decelerate evaporation for a given relative humidity, droplet size, and liquid water mass.

Figure 3 illustrates how the peak amplitude (p_+) of the trailing wave of the infrasonic emission varies with relative humidity, liquid water mass, droplet size, and air temperature. In general, the numerical values correspond to pressure perturbations at $x = 10$ km from the center of a cloud of radius $\epsilon = 100$ m. Sensibly, increasing the relative humidity to 100% damps the wave amplitude to

[3] Table 1 gives the unspecified parameters that are required to evaluate most curves in Figs. 2–4, for which $T_0 = 300$ K. For the exceptional cases where $T_0 = 275$ K, the pressure is reduced (dry adiabatically) to $p_0 = 10^5\ (275/300)^{c_p/R} = 73\ 757$ Pa; furthermore, the values of c_0, ρ_0, ψ, κ, r_{*0}, and $(\partial r_*/\partial T)_0$ are adjusted according to standard formulas (e.g., Pruppacher and Klett 1997; Emanuel 1994).

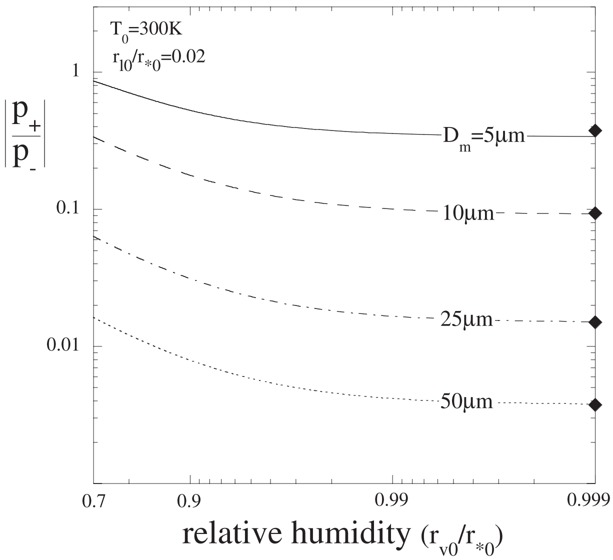

FIG. 4. Variation of the wave asymmetry ($|p_+/p_-|$) with RH and mean droplet size. The air temperature and the liquid mixing ratio (relative to r_{*0}) are specified on the plot. The cloud radius ϵ is 100 m. The diamonds on the right axis mark the approximate saturation limits for each curve, given by Eq. (45).

zero. Decreasing the liquid water mass also leads to a weaker emission. Increasing the droplet size decreases the trailing wave amplitude asymptotically as D_m^{-4}, assuming that $\beta = 3$. Lowering the air temperature (with an adiabatic pressure drop) also attenuates the wave, for a given relative humidity, droplet size, and liquid water mass.

Figure 4 illustrates how the trailing wave amplitude varies relative to the leading wave amplitude as the ambient water vapor and droplet size increase. Evidently, the magnitude of p_+/p_- tends toward a constant value as the relative humidity tends toward 100%. From Eq. (41), we obtain the following approximation for this value:

$$\left|\frac{p_+}{p_-}\right| \to \frac{4}{3}\frac{\epsilon}{c_0}\frac{1+b}{1+a}\mu_0 r_{l0}. \qquad (45)$$

Equation (41) also predicts the readily seen decay of p_+/p_- with increasing droplet size (as D_m^{-2} if $\beta = 3$).

The paradigm of infrasound generated by the evaporation of an isolated cloud, suddenly introduced into a subsaturated environment, was conceived for the purpose of testing c-RAMS. It does not adequately represent evaporation in a realistic storm, which may result from turbulent mixing or falling hydrometeors.[4] Nevertheless, the results shown here provide some basis for estimating the influence of evaporation (or condensation) on the infrasound in a storm simulation. We are primarily interested in the 0.1–10-Hz component of the infrasound, where severe storm signals are relatively strong and may contain detectable signatures of tornadoes (Bedard 2005). At 10 km from the source, the observed signals have wave amplitudes of the order 0.1 Pa (Bedard 2005; Schecter et al. 2008). The plots shown here loosely suggest that evaporation over 100-m-scale regions of high relative humidity (>90%) may noticeably affect these signals only if the cloud water has a mean droplet size of about 10 μm or less, or a liquid mixing ratio greater than 0.1 g kg^{-1}. Otherwise, phase transitions are too slow and the acoustic emissions are too weak.

b. *Comparison with c-RAMS*

Figure 5 compares the analytical pressure perturbations of section 4a with the infrasound simulated by c-RAMS due to evaporation under humid conditions. For proper comparison, all three numerical experiments use the single-moment parameterization in which D_m is held fixed. Table 1 lists the common parameters of all experiments (note that Table 1 neglects very small corrections to the ambient mass density and sound speed, associated with finite relative humidity), whereas Table 2 (rows 4–6) lists the distinguishing parameters. The left and middle plots correspond to simulations with the same relative humidity and liquid mixing ratio, but different values of D_m. The middle and right plots correspond to simulations with the same D_m, but different relative humidities and liquid mixing ratios.

Regardless of the specific conditions, the infrasonic emissions simulated by c-RAMS (solid curves) compare favorably to the analytical predictions (dotted curves) that are given by Eq. (39). We conclude that c-RAMS properly simulates the infrasound of parameterized evaporation in a humid environment.

5. Conclusions

In this paper, we derived analytical formulas for the infrasound generated by evaporating clouds in dry and humid environments. The derivations were based on the dynamical core of c-RAMS and standard single-moment microphysics parameterizations. The theoretical development elucidated the fundamental mechanism by which (liquid–vapor) phase transitions produce infrasound in the model. Furthermore, it explained the potential variation of 0.1–10-Hz emissions with the selected microphysics parameterization.

[4] In a practical storm simulation, the subgrid turbulence parameterization may have a switch that turns on when the local Richardson number is sufficiently small. Once activated, the model could rapidly mix finescale inhomogeneities of the entropy and moisture variables. Conceivably such mixing could (artificially) trigger the type of sudden phase transition considered here.

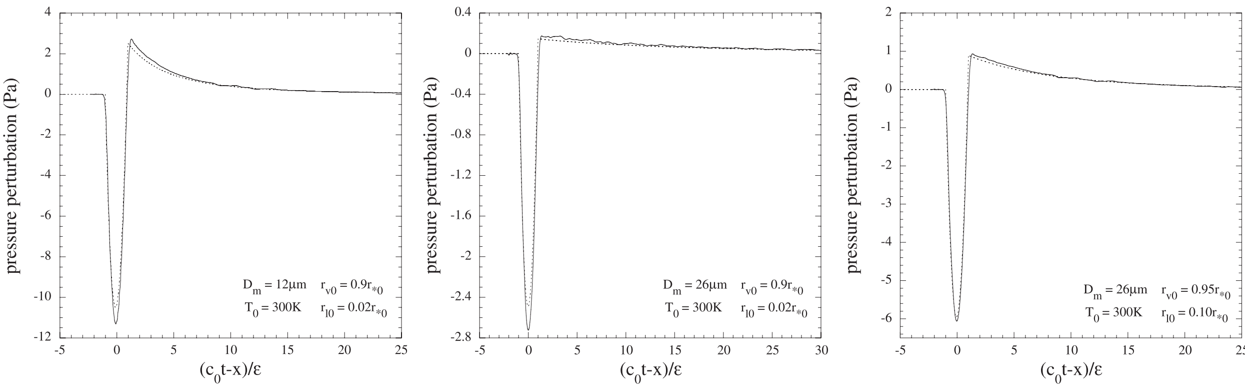

FIG. 5. Infrasound generated by evaporating clouds under humid conditions. The solid and dotted curves correspond to c-RAMS and theoretical predictions, respectively. The distinguishing characteristics of each experiment (and the common temperature) are printed in the lower-right corner of each plot. The pressure perturbations are multiplied by $\tilde{x} \equiv x/\epsilon$.

More important is that the analytical solutions gave us a benchmark for evaluating the ability of c-RAMS to simulate infrasound consistent with theory. Successful comparisons between the analytical results and computational output verified the adequacy of the numerics, under both dry and humid conditions. A more general theoretical benchmark covering the infrasound of ice and mixed-phase hydrometeors was left for another study. Nevertheless, appendix B shows that c-RAMS correctly generates the infrasound of an equilibrating cloud of mixed-phase hydrometeors, under the assumption that the microphysics algorithm properly models the ice–liquid–vapor phase conversions.

In summary, we have demonstrated that c-RAMS is built upon a solid foundation for simulating the infrasound associated with phase transitions of moisture. Fine details of the acoustic power spectrum (between 0.1 and 10 Hz) may vary with the microphysics parameterization, because phase transition rates are influenced by the imposed constraints on hydrometeor distributions. In our view, the subtle variation of spectral details should not discourage researchers from using c-RAMS (or any other cloud model) to investigate the conditions under which tornado infrasound may dominate the infrasound of generic moist processes within a storm. However, microphysics sensitivity tests may be necessary to establish definitive conclusions.

Acknowledgments. The authors thank Stephen Saleeby for a helpful discussion regarding the microphysics parameterizations in RAMS. The authors also thank three anonymous reviewers for their constructive comments on the original manuscript. This work was supported by NSF Grant ATM-0832320.

APPENDIX A

Customization of RAMS

In RAMS, the mass continuity equation is replaced with a prognostic equation for the Exner function, defined by $\Pi \equiv c_p(p/p_0)^{R/c_p}$. The complete form of this equation (including a term connected to mass exchange between air and hydrometeors) is given by

$$\partial_t \Pi' + \frac{c_0^2}{\rho_0 \theta_{v0}^2} \nabla \cdot (\rho_0 \theta_{v0} \mathbf{u}) = -\mathbf{u} \cdot \nabla \Pi' - \frac{R}{c_v} \Pi' \nabla \cdot \mathbf{u} + \frac{c^2}{\theta_v^2} \frac{d\theta_v}{dt} + \frac{c^2}{\theta_v(1 + r_v)} \frac{dr_v}{dt}, \tag{A1}$$

in which Π' is the perturbation Exner function and $c^2 \equiv R\Pi\theta_v/c_v$. All terms in Eq. (A1) are kept in the customized version of RAMS that is used here to study atmospheric acoustics (cf. Nicholls and Pielke 2000). The standard version of RAMS neglects the entire right-hand side.

Note that while perhaps unnecessary, the sedimentation routine was commented out of the code for this study. Furthermore, the macroscopic diffusion coefficients (connected to subgrid eddies) were given negligible values.

APPENDIX B

Linearized Pressure Equation with Ice

The linearized heat equation [Eq. (7)] is readily generalized to include ice and mixed-phase hydrometeors as follows:

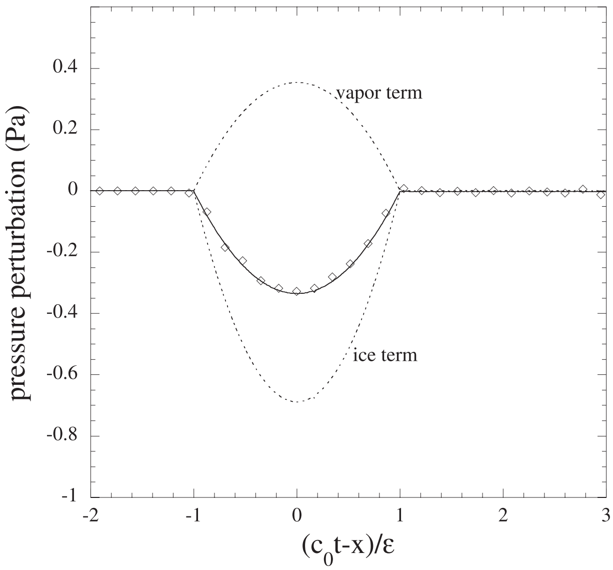

FIG. B1. Infrasound generated by suddenly introducing hail into warm, saturated air. The dotted curves are the theoretical waves produced by the vapor and ice source terms on the right-hand side of Eq. (B3). The solid curve is the combined wave, and the diamonds represent the infrasound simulated by c-RAMS. As usual, the pressure perturbation is multiplied by $\tilde{x} \equiv x/\epsilon$.

$$\partial_t \theta'_v = 0.61\theta_{v0}\partial_t r'_v + \theta_{v0}\frac{L_{\mathrm{lv}}\partial_t r'_l + L_{\mathrm{iv}}\partial_t r'_i}{c_p \max\{T_0, 253\,\mathrm{K}\}}. \tag{B1}$$

Neglecting diffusion by subgrid eddies and sedimentation, conservation of water mass implies that

$$r'_l = -r'_v - r'_i. \tag{B2}$$

Taking the time derivative of Eq. (2), and eliminating $\mathbf{u}$, ρ', θ'_v, and r'_l with Eqs. (3), (5), (B1), and (B2) yields

$$\partial_{tt}p' - c_0^2\nabla^2 p' = \rho_0 c_0^2\left(1.61 - \frac{L_{\mathrm{lv}}}{c_p \max\{T_0, 253\,\mathrm{K}\}}\right)\partial_{tt}r'_v + \rho_0 c_0^2 \frac{L_{\mathrm{iv}} - L_{\mathrm{lv}}}{c_p \max\{T_0, 253\,\mathrm{K}\}}\,\partial_{tt}r'_i. \tag{B3}$$

Given the time series of r_v and r_i, the solution of (B3) outside of a uniform cloud reduces to an integral similar to the right-hand side of Eq. (23).

Figure B1 verifies that the integral for p' agrees with the infrasound generated by c-RAMS, when a uniform sphere of hail ($\epsilon = 200$ m) is suddenly introduced into a warm ($T_0 = 300$ K) and saturated ($r_{v0} = r_{*0}$) environment. The experiment employs a single-moment parameterization in which the mean diameter (D_m) of the hail distribution is held constant at 1 cm, and $\nu = 2$. The initial value of the hail mixing ratio is 1.14 g kg^{-1}, and the initial liquid mass fraction is zero. Over time, the ice melts under the actions of heat and vapor diffusion, as explained in standard textbooks (e.g., Pruppacher and Klett 1997). Because the mean surface-to-volume ratio of hail is relatively small, phase transitions occur slowly. Consequently, the only significant infrasound is produced by the initial shock. The dotted curves show the individual contributions to the "shock wave" computed from the output vapor and ice (top and bottom) terms on the right-hand side of (B3). The solid curve is the sum of both contributions, which matches the pressure perturbation generated by c-RAMS (diamonds).

Note that the time step (dt_i) for the hail simulation is 2 ms, and the standard value of $L_{\mathrm{iv}} = 2.834 \times 10^6$ J kg^{-1} is used to calculate the theoretical infrasound.

APPENDIX C

Approximations in the Evaporation Equation under Humid Conditions

Equation (32) provides an approximation for the air temperature T that is derived from the following reformulated heat equation [Eq. (7)]:

$$\partial_t T' = -\frac{L_{\mathrm{lv}}}{c_p}\partial_t r'_v + \frac{RT_0}{c_p p_0}\partial_t p'. \tag{C1}$$

For a humid environment, we may assume that the evaporation rate E is sufficiently small for the acoustic wavelength c_0/E to greatly exceed the length scale l of the source region. Under this condition, Eq. (8) suggests that $p' \sim l^2E^2\rho_0 L_{\mathrm{lv}} r'_v/c_p T_0$. Accordingly, the ratio of the p' term over the r'_v term in Eq. (C1) is of the order $(l^2E^2/c_0^2)(R/c_v) \ll 1$. For this reason, Eq. (32) neglects the partial variation of T' with p'.

Equation (32) also provides an approximation for the hydrometeor temperature T_c. This formula assumes that $dT_c \equiv T_c - T_0$ is very small. From the relations

$$r_* = \frac{R}{R_v}\frac{e_*}{p - e_*} \quad \text{and} \quad \frac{de_*}{dT} = \frac{L_{\mathrm{lv}}e_*}{R_v T^2}, \tag{C2}$$

we obtain

$$dT_c = \frac{R_v T_0^2}{L_{\mathrm{lv}}p_0}\left(\frac{p_0 - e_{*0}}{r_{*0}}\,dr_{*c} + dp\right), \tag{C3}$$

in which R_v (R) is the gas constant of water vapor (dry air) and $e_*(T) \ll p$ denotes the saturation vapor pressure (e.g., Emanuel 1994). Using Eq. (33) to evaluate $dr_{*c} \equiv r_{*c} - r_{*0}$, and using our previous estimate of $dp \equiv p'$, one may show that neglecting the term proportional to dp in Eq. (C3) is typically consistent.

REFERENCES

Akhalkatsi, M., and G. Gogoberidze, 2009: Infrasound generation by tornadic supercell storms. *Quart. J. Roy. Meteor. Soc.,* **135,** 935–940.

Bedard, A. J., Jr., 2005: Low-frequency atmospheric acoustic energy associated with vortices produced by thunderstorms. *Mon. Wea. Rev.,* **133,** 241–263.

——, B. W. Bartram, A. N. Keane, D. C. Welsh, and R. T. Nishiyama, 2004: The infrasound network (ISNet): Background, design details, and display capability as an 88D adjunct tornado detection tool. Preprints, *22nd Conf. on Severe Local Storms,* Hyannis, MA, Amer. Meteor. Soc., 1.1. [Available online at http://ams.confex.com/ams/pdfpapers/816561.pdf.]

Cotton, W. R., and Coauthors, 2003: RAMS 2001: Current status and future directions. *Meteor. Atmos. Phys.,* **82,** 5–29.

Emanuel, K. A., 1994: *Atmospheric Convection*. Oxford University Press, 580 pp.

Georges, T. M., 1976: Infrasound from convective storms. Part II: A critique of source candidates. NOAA Tech. Rep. ERL 380-WPL 49, 59 pp. [Available from the National Technical Information Service, 5285 Port Royal Rd., Springfield, VA 22161.]

Klemp, J. B., and R. B. Wilhelmson, 1978: The simulation of three-dimensional convective storm dynamics. *J. Atmos. Sci.,* **35,** 1070–1093.

Meyers, M. P., R. L. Walko, J. Y. Harrington, and W. R. Cotton, 1997: New RAMS cloud microphysics parameterization. Part II: The two-moment scheme. *Atmos. Res.,* **45,** 3–39.

Nicholls, M. E., and R. A. Pielke Sr., 1994a: Thermal compression waves I: Total energy transfer. *Quart. J. Roy. Meteor. Soc.,* **120,** 305–332.

——, and ——, 1994b: Thermal compression waves II: Mass adjustment and vertical transfer of total energy. *Quart. J. Roy. Meteor. Soc.,* **120,** 333–359.

——, and ——, 2000: Thermally induced compression waves and gravity waves generated by convective storms. *J. Atmos. Sci.,* **57,** 3251–3271.

Passner, J. E., and J. M. Noble, 2006: Acoustic energy measured in severe storms during a field study in June 2003. Army Research Laboratory Tech. Rep. ARL-TR-3749, 42 pp.

Pruppacher, H. R., and J. D. Klett, 1997: *Microphysics of Clouds and Precipitation*. Kluwer Academic, 954 pp.

Saleeby, S. M., and W. R. Cotton, 2004: A large-droplet mode and prognostic number concentration of cloud droplets in the Colorado State University Regional Atmospheric Modeling System (RAMS). Part I: Module descriptions and supercell test simulations. *J. Appl. Meteor.,* **43,** 182–195.

Schecter, D. A., M. E. Nicholls, J. Persing, A. J. Bedard Jr., and R. A. Pielke Sr., 2008: Infrasound emitted by tornado-like vortices: Basic theory and a numerical comparison to the acoustic radiation of a single-cell thunderstorm. *J. Atmos. Sci.,* **65,** 685–713.

Szoke, E. J., A. J. Bedard Jr., E. Thaler, and R. Glancy, 2004: A comparison of ISNet data with radar data for tornadic and potentially tornadic storms in northeast Colorado. Preprints, *22nd Conf. on Severe Local Storms,* Hyannis, MA, Amer. Meteor. Soc., 1.2. [Available online at http://ams.confex.com/ams/pdfpapers/81466.pdf.]

Tripoli, G. J., and W. R. Cotton, 1981: The use of ice-liquid potential temperature as a thermodynamic variable in deep atmospheric models. *Mon. Wea. Rev.,* **109,** 1094–1102.

Walko, R. L., W. R. Cotton, M. P. Meyers, and J. Y. Harrington, 1995: New RAMS cloud microphysics parameterization. Part 1: The single-moment scheme. *Atmos. Res.,* **38,** 29–62.

——, ——, G. Feingold, and B. Stevens, 2000: Efficient computation of vapor and heat diffusion between hydrometeors in a numerical model. *Atmos. Res.,* **53,** 171–183.